# Electrocatalytic reduction of $CO_2$ to ethylene and ethanol through hydrogen-assisted C−C coupling over fluorine-modified copper

**Wenchao Ma[1,3], Shunji Xie[1,3], Tongtong Liu[1,3], Qiyuan Fan[1], Jinyu Ye[1], Fanfei Sun[2], Zheng Jiang[2], Qinghong Zhang[1]*, Jun Cheng[1]* and Ye Wang[1]***

[1]State Key Laboratory of Physical Chemistry of Solid Surfaces, Collaborative Innovation Center of Chemistry for Energy Materials, National Engineering Laboratory for Green Chemical Productions of Alcohols, Ethers and Esters, College of Chemistry and Chemical Engineering, Xiamen University, Xiamen 361005, China.

[2]Shanghai Synchrotron Radiation Facility, Shanghai Institute of Applied Physics, Chinese Academy of Sciences, Shanghai 201204, China.

[3]These authors contributed equally: Wenchao Ma, Shunji Xie, Tongtong Liu.

*e-mail: zhangqh@xmu.edu.cn; chengjun@xmu.edu.cn; wangye@xmu.edu.cn

**Electrocatalytic reduction of $CO_2$ into multi-carbon ($C_{2+}$) products is a highly attractive route for $CO_2$ utilization. However, the yield of $C_{2+}$ products remains low because of the limited $C_{2+}$ selectivity at high $CO_2$ conversion rate. Here, we report a fluorine-modified copper catalyst that exhibits an ultrahigh current density of 1.6 A $cm^{-2}$ at $C_{2+}$ (mainly ethylene and ethanol) Faradaic efficiency of 80% for electrocatalytic $CO_2$ reduction in a flow cell. The $C_{2-4}$ selectivity reaches 85.8% at a single-pass yield of 16.5%. We show a hydrogen-assisted C−C coupling mechanism between adsorbed formyl (CHO) intermediates for $C_{2+}$ formation. Fluorine enhances water activation, CO adsorption and hydrogenation of adsorbed CO to CHO intermediate that can readily undergo coupling. Our findings offer an opportunity to design highly active and selective $CO_2$ electroreduction catalysts with potential for practical application.**

The transformation of $CO_2$ into fuels and chemicals has great potential to mitigate the depletion of fossil resources and abate carbon emissions[1-3]. The synthesis of multi-carbon ($C_{2+}$) products such as ethylene and ethanol from $CO_2$ is highly attractive because of the versatility of these products in the chemical and energy industries[4-8]. Catalytic hydrogenation of $CO_2$ with $H_2$ could produce $C_{2+}$ products at high temperatures and pressures, but this thermocatalytic conversion of $CO_2$ suffers from wide distributions of $C_{2+}$ products as well as the formation of $CH_4$ and CO[5-9]. The control of C−C coupling is a critical challenge in thermocatalytic hydrogenation of $CO_2$ due to the uncontrollable polymerization mechanism on heterogeneous catalysts[5-8]. Electrocatalytic $CO_2$ reduction reaction ($CO_2RR$) with water using renewable electricity offers a promising route for $CO_2$ utilization under ambient conditions[10-12]. Better control of $C_{2+}$ products via electrocatalytic $CO_2RR$ may be possible because the C−C coupling on electrocatalysts proceeds via mechanism different from that in thermocatalytic reactions[13−15]. Despite recent progress in electrocatalytic $CO_2RR$ to $C_{2+}$ products[15-17], the reaction still suffers from limited $C_{2+}$ selectivity at high activity. The $C_{2+}$ yield by electrocatalytic $CO_2RR$ is generally lower than those reported for thermocatalysis.

Copper is known to be the most selective catalyst for electrocatalytic $CO_2RR$ to $C_{2+}$ products[15-17]. Several strategies such as morphology and facet enginnering[18-20], vacancy steering[21], dopant modification[22], bimetallic catalysis[23-26], and electrolyte design[27-30] have been developed to enhance the efficiency of Cu catalyst for $C_{2+}$ formation. Although high Faradaic efficiencies (FEs) of $C_{2+}$ products have been reported, the activity remains low and the operation window is narrow in most cases. Several studies have succeeded in obtaining high current densities (> 100 mA $cm^{-2}$) for $CO_2RR$ to $C_{2+}$ products using flow cell with gas diffusion

electrode (GDE) to overcome the $CO_2$ solubility limit in aqueous solution[19,25,28,30,31]. More efficient electrocatalysts that meet the commercial purpose still remain to be developed.

Here, we report a fluorine-modified Cu catalyst, which shows a $C_{2+}$ (mainly ethylene and ethanol) FE of 80% at current density of 1.6 A $cm^{-2}$ during electrocatalytic $CO_2$RR in a flow cell, resulting in a $C_{2+}$ formation rate of ~4.0 mmol $h^{-1}$ $cm^{-2}$, significantly higher than those reported to date. The selectivity and single-pass yield of $C_{2-4}$ products reach 85.8% and 16.5%, respectively, which outperform those reported for thermocatalytic hydrogenation of $CO_2$ under harsh conditions. Our studies suggest an alternative mechanism for C−C coupling between adsorbed formyl species (*CHO) on Cu surfaces. The presence of fluorine promotes water dissociation, CO adsorption and the formation of ∗CHO intermediates.

## Results

### Electrocatalytic $CO_2$RR on halogen-modified Cu catalysts

We fabricated the fluorine-modified Cu catalyst by electroreduction of a Cu(OH)F precursor, which was synthesized by a solvothermal method. The anion exchange of Cu(OH)F with ammonium halide ($NH_4Cl$, $NH_4Br$ or $NH_4I$) followed by electroreduction provided other halogen-modified Cu catalysts. The obtained catalysts were denoted as X−Cu (X = F, Cl, Br or I). The Cu catalyst without halogen was fabricated by a similar method. A flow cell with GDE (Supplementary Fig. 1) was designed for electrocatalytic $CO_2$RR to enable the direct feeding of gaseous $CO_2$ to the electrode-electrolyte interface to circumvent the transport limitation of $CO_2$.

We measured linear sweep voltammetry (LSV) for the X−Cu catalysts under both $CO_2$ and

Ar atmospheres. The current density increased with the electronegativity of halogen[32] in the catalyst under both atmospheres (Supplementary Fig. 2). Under $CO_2$ atmosphere, the cathodic current density was significantly higher than that under $N_2$ for each catalyst. These results suggest that the F−Cu catalyst is the most active for $CO_2$RR.

Electrocatalytic performances of X−Cu catalysts for $CO_2$RR were evaluated at different cathodic potentials in 1.0 M KOH electrolyte. $H_2$, CO, formate, $CH_4$ and $C_{2+}$ products were formed on pristine Cu, and the modification of Cu with halogen significantly decreased FEs of $H_2$ and $C_1$ products and increased that of $C_{2+}$ products (Supplementary Fig. 3a-e). Ethylene and ethanol were the major $C_{2+}$ products together with minor acetate and *n*-propanol. The X–Cu catalysts all exhibited a volcano-shaped dependence of $C_{2+}$ FE on applied potential and the maximum $C_{2+}$ FE values were observed at −0.6 to −0.8 V versus reversible hydrogen electrode (RHE) (Fig. 1a). Both the FEs and formation rates of $C_{2+}$ products increased significantly with the electronegativity of X in the X−Cu catalysts at all potentials applied, and the best performance was achieved over the F−Cu catalyst (Fig. 1a,b). The change in applied potential from −0.22 to −0.67 V versus RHE for this catalyst led to a variation in current density in a broad range from 13 to 800 mA $cm^{-2}$ and the current density remained stable during the electrocatalysis at each applied potential (Supplementary Fig. 3f). We further normalized the $C_{2+}$ formation rate based on the electrochemical surface area (ECSA), which was determined by the double-layer capacitance method (Supplementary Fig. 4a and Supplementary Table 1). The normalized $C_{2+}$ formation rates also increased in the sequence of Cu < I−Cu < Br−Cu < Cl−Cu < F−Cu at all the applied potentials investigated (Supplementary Fig. 4b).

Electrocatalytic $CO_2$RR over the F−Cu catalyst in KOH electrolytes with different

concentrations showed that a higher KOH concentration favoured the activity and $C_{2+}$ FE at a lower applied potential (Supplementary Fig. 5a-c). In 2.5 M KOH, the current density was 400 mA $cm^{-2}$ at −0.48 V versus RHE. Higher $C_{2+}$ FEs (≥ 80%) were obtained at applied potentials of ≤ −0.62 V versus RHE in 2.5 M KOH. The $C_{2+}$ formation rates reached 1007, 2070 and 3050 μmol $h^{-1}$ $cm^{-2}$ with current densities of 400, 800 and 1200 mA $cm^{-2}$ at −0.48, −0.54 and −0.62 V versus RHE, respectively (Fig. 1c). Thus, the operation window to gain a high $C_{2+}$ FE (≥ 80%) for our catalyst is quite wide. A further increase in the applied potential decreased the $C_{2+}$ FE in 2.5 M KOH. On the other hand, the $C_{2+}$ FE could keep at ≥ 80% at higher applied potentials in KOH with a lower concentration. In 0.75 M KOH, the $C_{2+}$ FE was 80% at −0.89 V versus RHE with a current density of 1600 mA $cm^{-2}$ (Supplementary Fig. 5a), and the $C_{2+}$ formation rate reached 4013 μmol $h^{-1}$ $cm^{-2}$ (Fig. 1c). The formation rate and FE of ethylene alone were 3234 μmol $h^{-1}$ $cm^{-2}$ and 65%, respectively. It is noteworthy that both the $C_{2+}$ and ethylene formation rates are the highest reported to date for electrocatalytic $CO_2$RR. We evaluated the half-cell energy conversion efficiency (ECE) for $C_{2+}$ products, which was calculated by using the ratio of chemical energy stored in the $C_{2+}$ products versus input electrical energy needed to implement the reaction[10]. Our F−Cu catalyst demonstrated $C_{2+}$ ECEs of ≥ 55% with current densities of 400 and 800 mA $cm^{-2}$ at −0.48 and −0.54 V versus RHE (Supplementary Fig. 5d), suggesting that most of electrical energy is used to produce $C_{2+}$ products under such conditions. In addition, we assembled a full cell system with a Ni foam@$NiFeO_x$ nanosheet catalyst (Supplementary Fig. 6a,b) as the anode for oxygen evolution and the F−Cu catalyst as the cathode catalyst for $CO_2$RR. The system delivered a full-cell ECE for $C_{2+}$ products of 37% with current density of 132 mA $cm^{-2}$ at a cell voltage of 2.4 V in 2.5

M KOH (Supplementary Fig. 6c,d). We have compared the $CO_2$RR-to-$C_{2+}$ electrocatalytic performance of the F−Cu catalyst with those of other top catalysts reported so far (Fig. 1d). The F−Cu catalyst can achieve significantly higher activity at a $C_{2+}$ FE of ≥ 80% than the reference catalysts even with the flow cell. The $C_{2+}$ ECE value of the F−Cu catalyst is also superior to those reported for other catalysts (Supplementary Table 2).

At a fixed current density of 1600 mA $cm^{-2}$ in 0.75 M KOH electrolyte, the $C_{2+}$ FE was lower at a lower $CO_2$ flow rate due to $H_2$ formation and the increase in $CO_2$ flow rate to 20 mL $min^{-1}$ significantly increased $C_{2+}$ FE (Supplementary Fig. 7a). The $CO_2$ conversion and $C_{2+}$ selectivity on a molar carbon basis, which are usually used to express the performance of a heterogeneous catalyst, increased with $CO_2$ flow rate up to 20 mL $min^{-1}$ (Supplementary Fig. 7b). The $CO_2$ conversion decreased with a further increase in $CO_2$ flow rate. The highest $CO_2$ conversion was 19.3%. The $C_{2+}$ selectivity and single-pass $C_{2+}$ yield were 85.8% and 16.5%, respectively, at the same time. The selectivities of $C_2H_4$ and ethanol were 65.2% and 15.0%, respectively. The yield of $C_2H_4$ reached 12.4%. It is noteworthy that such a high selectivity (80.2%) of $C_2$ products ($C_2H_4$ and ethanol) can hardly be achieved in the hydrogenation of $CO_2$ over conventional heterogeneous catalysts[5-9]. The comparison with typical $CO_2$ hydrogenation heterogeneous catalysts demonstrates that the present electrocatalytic system is significantly more selective toward $C_{2-4}$ products, in particular $C_2H_4$ and ethanol, on a comparable or higher level of $C_{2-4}$ yield (Fig. 1d). The space time yield of $C_{2-4}$ products reached ~35.5 mol $g_{cat}^{-1}$ $h^{-1}$ over the F−Cu electrocatalyst, which is about three orders of magnitude higher than those for $CO_2$ hydrogenation over typical heterogeneous catalysts (Supplementary Table 3).

Although the alkaline GDE is very effective for electrocatalytic $CO_2$RR[17,28,30,33], the long-

term stability remains challenging. It is generally believed that the GDE suffers from losing hydrophobicity and being flooded over time[28,33]. To overcome the loss of hydrophobicity and the salt accumulation, we modified the GDE with fluoroalkyl silane (1H,1H,2H,2H-perfluorooctyltrichlorosilane)[34] and refreshed the electrolyte every 8 h. Considering that the $C_{2+}$ FE at a current density of 400 mA $cm^{-2}$ was high and the flooding of the GDE occurred at a higher current density even after the modification with fluoroalkyl silane (Supplementary Fig. 8a), we chose the current density of 400 mA $cm^{-2}$ for stability test. Our F−Cu catalyst showed superior stability and no significant changes in performances were observed in 40 h of operation at a constant current density of 400 mA $cm^{-2}$ (Supplementary Fig. 8b). To the best of our knowledge, few studies can achieve such long-term stability for $CO_2$RR to $C_{2+}$ products at a current density of >100 mA $cm^{-2}$. Therefore, the present F−Cu electrocatalyst is very promising for the direct transformation of $CO_2$ into $C_{2+}$ products, in particular ethylene and ethanol.

**Characterization of halogen-modified Cu catalysts**

Our X-ray diffraction (XRD) measurements clarified that Cu(OH)F was formed after the solvothermal synthesis. The exchange with other halide anions led to crystalline $Cu_2(OH)_3Cl$, $Cu_2(OH)_3Br$ and CuI phases (Supplementary Fig. 9). The electroreduction of these precursors all resulted in metallic Cu as the sole crystalline phase (Supplementary Fig. 10). The scanning electron microscopy (SEM) showed that all the catalysts had the same particulate morphology (Fig. 2a and Supplementary Fig. 11a-e). The average diameters of Cu particles in these catalysts were similar (102-136 nm) (Supplementary Fig. 12a-e). After 40 h of stability test, the

morphology and the mean size of Cu in the F−Cu catalyst maintained almost unchanged (Supplementary Figs. 11f and 12f). The high-resolution transmission electron microscopy (HRTEM) results displayed lattice fringes with an interplanar spacing of 0.208 nm for all catalysts (Fig. 2b and Supplementary Fig. 13a-e), which could be ascribed to the Cu(111) facet[35]. No additional crystalline phases were observed after reaction (Supplementary Fig. 13f). These results indicate that the crystalline structure and the morphology of our catalysts are not the crucial factors that determine the electrocatalytic $CO_2$RR performance.

The F 1s spectrum from X-ray photoelectron spectroscopy (XPS) for the F−Cu catalyst displayed a peak at 685 eV, which could be assigned to $F^-$ in fluoride[36] (Fig. 2c). The XPS studies confirmed that no fluorine species remained on the Cl−Cu, Br−Cu and I−Cu catalysts (Supplementary Fig.14), which were fabricated by anionic exchange of Cu(OH)F followed by electroreduction, whereas $Cl^-$, $Br^-$or $I^-$ species existed on the surfaces of these catalysts[37] (Supplementary Fig. 15). The surface halogen contents measured by XPS for the X−Cu catalysts were ~6 mol%, significantly higher than their bulk contents (~2 mol%) measured by the energy-dispersive X-ray (EDX) analysis (Supplementary Fig. 16a,b). The sputtering of the F−Cu sample before or after reaction with Ar ions resulted in a drastic decrease in the intensity of F signal in XPS spectrum (Supplementary Fig. 17). These results suggest that the halogen species are mainly located at the surface region of Cu particles. The binding energies of Cu $2p_{3/2}$ for the X−Cu catalysts were all around 932.5 eV (Supplementary Fig. 18a), which could be attributed to that of either $Cu^0$ or $Cu^+$. The Cu LMM Auger spectra clarified that $Cu^0$ (918.5 eV) and $Cu^+$ (916.5 eV) species co-existed on X−Cu catalysts[35] (Fig. 2d). The O 1s spectra displayed that some oxidized species were also present on the surfaces of X−Cu catalysts[26]

(Supplementary Fig. 18b). The XPS results for the F−Cu catalyst after stability test revealed that the chemical states of fluorine, copper and oxygen on surfaces did not undergo significant changes during long-time operation (Supplementary Fig. 19). The surface F content remained unchanged at ~6 mol% in the initial 1 h of $CO_2$RR and decreased progressively to ~4 mol% after 40 h of reaction (Supplementary Fig. 16c). We further performed *in situ* X-ray absorption spectroscopy (XAS) measurements for the X−Cu catalysts at −0.6 V versus RHE. The comparison in Cu K-edge adsorption of the X−Cu catalysts with the reference samples suggests that the average oxidation states of Cu in the X−Cu catalysts lie between 0 and +1 under reaction conditions (Fig. 2e). The average oxidation state of Cu increased with the electronegativity of halogen.

**Density functional theory calculations**

To gain insights into the reaction mechanism and the role of fluorine, we have performed density functional theory (DFT) calculations for $CO_2$RR to $C_2H_4$, the major $C_{2+}$ product, on Cu(111) and F-modified Cu(111) surfaces. Different from the boron-doped copper catalysts, where boron could be distributed into the subsurface region[22], it is energetically more favourable for fluorine to stay on the surface of Cu(111) slab than to diffuse into the subsurface by a margin of 1.16 eV (Supplementary Fig. 20). Thus, we used the configuration of F located at the surface site of Cu(111) for DFT calculation. The bond lengths and coordination numbers of Cu−F and Cu−Cu with F at Cu surface optimised by DFT calculations are very close to those obtained by the EXAFS fitting[38] (Supplementary Fig. 21 and Supplementary Table 4). The optimized structures of the key intermediates on Cu and F−Cu surfaces are displayed in

Supplementary Fig. 22.

Regarding the C−C coupling mechanism on Cu surfaces, the current consensus is that $CO_2$ is first reduced to form adsorbed CO and the adsorbed CO subsequently undergoes dimerization to adsorbed OCCO, which leads to the formation of $C_2H_4$[13,20-22]. Our DFT calculations confirmed that $CO_2$ could be easily converted to adsorbed CO (∗CO) via ∗COOH intermediate on both Cu and F−Cu surfaces. However, a high uphill reaction energy was required for the formation of ∗O∗CCO intermediate from ∗CO (~1.9 eV) on either Cu(111) or F−Cu(111) surface (Fig. 3a). This indicates that the C−C coupling through ∗CO dimerization is difficult. On the other hand, the reaction energy for the hydrogenation of ∗CO was significantly lower than that for the dimerization of ∗CO to ∗O∗CCO over both Cu and F−Cu surfaces. For the hydrogenation of ∗CO on Cu surface, the addition of ∗H species to carbon atom of ∗CO to form ∗CHO has a reaction energy of 0.79 eV (Fig. 3a), which is lower than that for the addition of ∗H species to oxygen of ∗CO to form ∗COH (1.07 eV) (Fig. 3b). The presence of F on Cu significantly decreased the reaction energy for the formation of ∗CHO from 0.79 to 0.48 eV, whereas such a decrease for the formation of ∗COH was insignificant (Fig. 3a,b). Therefore, ∗CHO other than ∗COH should be the major species from ∗CO hydrogenation on both surfaces. We have further investigated the effect of CO coverage on ∗O∗CCO and ∗CHO formations, which are believed to be more facile at high CO coverages[39-41]. The barrier for ∗CHO formation is significantly lower than the reaction energy for ∗O∗CCO formation at each CO coverage investigated on Cu(111) surface (Supplementary Note 1 and Supplementary Figs. 23-25), suggesting that the hydrogenation of ∗CO to ∗CHO is energetically more favourable than the dimerization of ∗CO to ∗O∗CCO.

We further studied C−C coupling between different $C_1$ species on Cu(111) and F−Cu(111) surfaces. As compared to ∗CO dimerization, which requires a high uphill reaction energy, the coupling between ∗CHO or ∗COH species to form ∗OCHCHO∗ or HOC∗∗COH intermediate is exergonic over both surfaces (Fig. 3a,b). Our DFT calculation indicates that the coupling between ∗CHO and ∗CO species is difficult because of the uphill reaction energies on both surfaces (Fig. 3c). The effect of electrolyte and the energy barriers of different pathways were also investigated. Although the reaction energies decreased in the presence of electrolyte, the trend remained the same. In other words, the hydrogenation of ∗CO to ∗CHO followed by the subsequent coupling of ∗CHO to ∗OCHCHO∗ is the most favourable pathway for the formation of $C_2H_4$ (Supplementary Figs. 26-28 and Supplementary Table 5).

In short, the DFT calculations suggest that the reduction of $CO_2$ to ∗CO via ∗COOH, followed by the hydrogenation of ∗CO to ∗CHO and the subsequent coupling of ∗CHO to ∗OCHCHO∗ is the most favourable pathway for the formation of $C_2$ products, in particular $C_2H_4$, over Cu(111) and F−Cu(111) surfaces. Nørskov and co-workers also found that the coupling between hydrogenated adsorbed species (∗$CH_xO$) showed lower barriers than the dimerization of adsorbed CO on Cu(211) surfaces[42]. Our DFT calculations further indicate that the fluorine modification may accelerate the hydrogenation of ∗CO to ∗CHO, and thus contributes to the enhanced $C_{2+}$ selectivity via coupling of ∗CHO.

**Functioning mechanism of fluorine**

It is noteworthy that halogen anions added in electrolyte may also promote $CO_2RR$[27,29]. The presence of KX in $KHCO_3$ electrolyte in an H-cell was found to increase the $CO_2RR$ current

density in the sequence of $Cl^- < Br^- < I^-$ over plasma-activated Cu catalyst, while the $C_{2+}$ FE remained unchanged at the same time[29]. We also found that when KX was added into electrolyte, the current density and $C_{2+}$ formation rate over Cu catalyst increased with a decrease in the electronegativity of halogen, while the $C_{2+}$ FE only changed slightly (Supplementary Fig. 29). Recently, Cuenya and co-workers found that the pretreatment of Cu foil in KX solution to form Cu_X catalysts containing surface halides could also increase the activity for $CO_2$RR in the H-cell in the sequence of $Cl^- < Br^- < I^-$[43]. However, the different catalyst morphologies, halide contents and ECSAs of the Cu_X catalysts make it difficult to disentangle the intrinsic role of surface halide species. On the other hand, our series of X−Cu catalysts had similar morphologies, halogen contents and ECSAs, offering a proper model system to elucidate the functions of surface halide species in $CO_2$RR to $C_{2+}$ compounds. Our results showed that both the formation rate and FE of $C_{2+}$ products increased significantly with the electronegativity of halogen species on catalyst surfaces. Therefore, the halogen species on catalyst surface and in electrolyte should work in different mechanisms for $CO_2$RR.

Tafel analyses for electrocatalytic $CO_2$RR to $C_2H_4$ on X−Cu catalysts show that the slope becomes lower in the presence of halogen and decreases upon increasing the electronegativity of halogen (Fig. 4a). This suggests that the rate-determining step for $C_2H_4$ formation may change with halogen modifier[28,44-46]. The electron transfer may be involved in the rate-determining step on Cu catalyst from its Tafel slope. In contrast, the Tafel slope for the F−Cu catalyst, which is close to 59 mV $dec^{-1}$, suggests that the electron transfer is faster and the subsequent chemical reaction becomes the rate-determining step.

To confirm that CO is a key intermediate during $CO_2$RR on our catalysts (Fig. 3a), we have

performed electrocatalytic reduction of CO under the same circumstance with that of $CO_2$. Similar to $CO_2$RR, electrocatalytic CO reduction provided $C_2H_4$ as the major product together with $H_2$, $CH_4$, ethanol, acetic acid and *n*-propanol on our catalysts (Supplementary Fig 30a). The FEs of $C_2H_4$ and total $C_{2+}$ products increased in the sequence of Cu < I−Cu < Br−Cu < Cl−Cu < F−Cu. Furthermore, the partial current density of $C_2H_4$ during electrocatalytic CO reduction was very close to that during $CO_2$RR (Supplementary Fig 30b). These observations provide evidence that electrocatalytic $CO_2$RR over our catalysts proceeds via CO intermediate.

We found that the onset potential of $C_2H_4$ in electrocatalytic $CO_2$RR over the X−Cu catalyst decreased significantly with an increase in the electronegativity of halogen, while that of CO only decreased slightly at the same time (Fig. 4b). This suggests that the halogen modification mainly promotes the reaction steps after ∗CO formation. The enhancement in CO adsorption is known to be important for obtaining high $C_{2+}$ selectivity, which helps to build up a sufficient ∗CO coverage for subsequent C−C coupling rather than desorption of CO as a product[22,27,28]. We clarified that CO adsorption capacity increased in the sequence of Cu < I−Cu < Br−Cu < Cl−Cu < F−Cu (Supplementary Fig. 31). The presence of $Cu^+$ sites on Cu catalysts may enhance CO adsorption[22]. Our XPS and XANES measurements revealed that the fraction of $Cu^+$ sites increased with the electronegativity of halogen in X−Cu catalysts (Fig. 2d,e). Thus, the enhanced CO adsorption on the catalyst modified by halogen with a larger electronegativity may contribute to the higher $C_{2+}$ selectivity. We further fabricated an oxide-derived Cu catalyst to decouple the specific role of fluoride species from the role of $Cu^+$ for $CO_2$RR. The results suggest that the presence of $Cu^+$ sites may partially account for the enhanced $CO_2$RR-to-$C_{2+}$ performance probably by enhancing CO adsorption (Supplementary Note 2 and Supplementary

Figs. 11g, 31-33). The significantly better performance of the F−Cu catalyst as compared to the oxide-derived Cu catalyst (Supplementary Fig. 33) as well as the positive effect of $F^-$ added to the electrolyte on the $C_{2+}$ FEs and formation rates of the Cl−Cu, Br−Cu and I−Cu catalysts (Supplementary Fig. 34) indicate that the fluoride species plays other roles in $CO_2RR$ to $C_{2+}$ products (Supplementary Note 2).

Our DFT calculations suggest that the hydrogenation of ∗CO may be the rate-determining step during the electrocatalytic $CO_2RR$ to $C_2H_4$ (Fig. 3a). The activation of $H_2O$ to active hydrogen species may thus be an important step. Actually, the $H_2O$ activation in alkaline medium is a slow step in $H_2$ evolution reaction (HER)[46]. Our previous work indicated that the formation of hydrogen species from $H_2O$ is a key step in electrocatalytic $CO_2RR$ to formate on a sulfur-modified indium catalyst[47]. To understand the role of $H_2O$ activation in electrocatalytic $CO_2RR$ to $C_{2+}$ products, we have measured the kinetic isotopic effect (KIE) of H/D over X−Cu catalysts. When $D_2O$ was used instead of $H_2O$ in 1.0 M KOH electrolyte, the formation rate of ethylene decreased, but the degree of such a decrease depended significantly on halogen in catalyst (Supplementary Fig. 35). The KIEs of H/D, which are defined as the ratio of ethylene formation rates in $H_2O$ and $D_2O$, were calculated to be 2.0, 1.8, 1.5, 1.3 and 1.2 over Cu, I−Cu, Br−Cu, Cl−Cu and F−Cu catalysts, respectively (Fig. 4c). The value of 2.0 over Cu catalyst is characteristic of primary KIE, indicating that the dissociation of $H_2O$ is involved in the rate-determining step[47]. In contrast, the KIE over the F−Cu catalyst becomes close to 1.0. The dissociation of $H_2O$ is no longer the rate-determining step over this catalyst. Therefore, the presence of $F^-$ on Cu accelerates $H_2O$ activation.

The adsorbed anionic species on metal surfaces may promote $H_2O$ dissociation via the

reaction of $H_2O + e^- \rightarrow OH^- + *H$[46-48]. It is proposed that the anionic species and the hydrated cation can form anion-hydrated cation ($K^+(H_2O)_n$) networks in the double layer through non-covalent Coulomb interactions, thus enhancing $H_2O$ activation to ∗H species. Under Ar atmosphere, the $H_2$ formation rate increased with an increase in the electronegativity of halogen in the X−Cu catalysts (Fig. 4c), confirming that halogen on Cu surfaces plays a role in $H_2O$ activation. We speculate that the increase in electronegativity would increase the interaction between halide anion and hydrated cation, thus enhancing $H_2O$ dissociation.

To gain further insights into the role of $H_2O$ activation in $CO_2RR$ to $C_{2+}$ products, we have investigated the effect of alkali metal (M) cations in MOH electrolyte. The hydrated cation of $M^+(H_2O)_n$ ($n$ = 13, 7 and 6 for $Na^+$, $K^+$ and $Cs^+$, respectively) with a smaller $n$ and radius is believed to have a stronger interaction with anionic species on metal surfaces and thus higher ability to activate $H_2O$[47]. Upon changing the cation from $Na^+$ to $Cs^+$, the HER performance was significantly enhanced over the F−Cu catalyst, while the enhancing effect over Cu catalyst was very limited (Supplementary Fig. 36a,b). For electrocatalytic $CO_2RR$ over the F−Cu catalyst, the $C_2H_4$ formation rate increased markedly from 428 to 721 μmol $h^{-1}$ $cm^{-2}$ upon changing the cation from $Na^+$ to $K^+$ (Fig. 4d and Supplementary Fig. 36c). A further change of the cation to $Cs^+$ rather decreased $C_2H_4$ formation rate due to increased formation of formate. This suggests that a too stronger $H_2O$ activation ability is unbeneficial to $C_2H_4$ formation but favours formate formation, a pathway parallel to the formation of ∗CO intermediate[47,49]. On the other hand, over Cu catalyst, which has a weaker $H_2O$ activation ability, the $C_2H_4$ formation rate increased only slightly upon changing the cation from $Na^+$ to $K^+$ and to $Cs^+$ (Fig. 4d and Supplementary Fig. 36d). This supports our speculation that $F^-$ on Cu surface enhances $C_2H_4$ formation by

promoting $H_2O$ activation through interaction with hydrated cations.

The effect of pH of electrolyte was also investigated to understand the role of $H_2O$ activation. The local pH at the cathode/electrolyte interface is known to increase in the sequence of $K_2HPO_4 < K_2CO_3 < K_2SO_4$[30,47], and thus the three electrolytes with a concentration of 0.5 M were employed to regulate the pH. Upon changing the electrolyte from $K_2HPO_4$ to $K_2CO_3$ and further to $K_2SO_4$, the $C_{2+}$ formation rate significantly increased over the F−Cu catalyst, whereas the rate enhancement over the Cu catalyst was very limited (Supplementary Fig. 37), suggesting that the role of $F^-$ species in enhancing $C_{2+}$ formation is more significant at a higher pH value. This result provides further evidence that the $F^-$ modification enhances $C_{2+}$ formation by accelerating the activation of $H_2O$, which becomes more difficult at a higher pH value[46-48].

We further conducted *in situ* electrochemical attenuated total reflection Fourier-transform infrared spectroscopy (ATR-FTIRS) measurements to characterise reaction intermediates. Upon scanning the applied potential from −0.1 to −0.3 V versus RHE over the F−Cu catalyst, three broad asymmetric IR bands appeared at 2117, 1972 and 1920 $cm^{-1}$ (Fig. 5a), attributable to electrogenerated CO bound to Cu surface[50-52]. The further scanning to −0.4 V versus RHE, a new band appeared at around 1754 $cm^{-1}$, which could be ascribed to the surface-bound CHO species[50], a key intermediate that we proposed for C−C coupling. The intensity of the IR band ascribed to the CHO species increased significantly upon scanning to more negative potentials, and this is consistent with the trend of $C_{2+}$ formation rates (Fig. 1b). On the other hand, the IR bands for CO over Cu catalyst did not appear until −0.4 V versus RHE, and the intensities were much lower than those over the F−Cu catalyst (Fig. 5b). We did not observe the IR band ascribed to the CHO species over Cu catalyst probably because the coverage of CHO species

was too low. This is consistent with the low $C_{2+}$ formation rates over the Cu catalyst. The ATR-FTIRS results provide experimental evidence for the hydrogen-assisted C−C coupling mechanism.

In short, our studies suggest a hydrogen-assisted C−C coupling mechanism, in which the adsorbed ∗CO and ∗CHO species are key intermediates (Fig. 5c and Supplementary Fig. 38). On Cu catalyst, $H_2O$ activation to ∗H species involving electron transfer is a slow step. The modification by fluorine promotes the $H_2O$ dissociation and the hydrogenation of ∗CO to ∗CHO species becomes the rate-determining step on the F−Cu catalyst. Fluorine also enhances CO adsorption by increasing surface $Cu^{\delta+}$ sites.

**Discussion**

We have discovered a highly active and selective fluorine-modified copper catalyst for electrocatalytic $CO_2$RR in flow cell using gas diffusion electrode to $C_{2+}$ products mainly composed of ethylene and ethanol. The F−Cu catalyst offers $C_{2+}$ products with Faradaic efficiency of 84% at current density of 800 mA $cm^{-2}$ at −0.54 V versus RHE. The energy conversion efficiency reaches 55%. At −0.89 V versus RHE, the current density reaches 1600 mA $cm^{-2}$ with $C_{2+}$ Faradaic efficiency of 80%. We have obtained a $C_{2+}$ formation rate of 4013 μmol $h^{-1}$ $cm^{-2}$, which is significantly higher than those reported to date. Furthermore, the $C_{2+}$ selectivity on the molar carbon basis reaches 85.8% (ethylene 65.2%, ethanol 15.0%) with a single-pass $C_{2+}$ yield of 16.5%. This combination of selectivity and yield is better than those reported for thermocatalytic hydrogenation of $CO_2$ under harsh reaction conditions.

We propose a hydrogen-assisted C−C coupling mechanism for electrocatalytic $CO_2$RR to $C_{2+}$

products on our halogen-modified Cu catalysts. The adsorbed CO and CHO species are key reaction intermediates. The activation of $H_2O$ to unique H species is an important step. The halogen modifier facilitates the activation of $H_2O$. The CO adsorption and the hydrogenation of adsorbed CO are also accelerated by halogen on Cu surfaces. The coupling of adsorbed CHO species can readily proceed on Cu surfaces.

## Methods

### Chemicals and materials

Copper nitrate trihydrate ($Cu(NO_3)_2 \cdot 3H_2O$), ammonium hydrogen difluoride ($NH_4HF_2$), ammonium chloride ($NH_4Cl$), ammonium bromide ($NH_4Br$), ammonium iodide ($NH_4I$), potassium hydroxide (KOH), deuterium water ($D_2O$) and 1H,1H,2H,2H-perfluorooctyltrichlorosilane were purchased from Energy Chemical Co. *N*,*N*-dimethyformamide (DMF), dimethylsulfoxide (DMSO), ethanol, isopropanol and toluene were purchased from Sinopharm Chemical Co. Gas diffusion layer (GDL, YLS-30T), Nafion binder (5 wt%, DuPont520), anion exchange membrane (NEOSEPTA, AHA) and Ni foam (thickness 1.0 mm) were purchased from Japanese Fuel Cell Store Co. The GDL was composed of carbon fiber in 0.19 mm thickness and hydrophobic microporous carbon in 0.04 mm thickness. The ultrapure water used in all experiments with a resistivity of 18.2 megohms was prepared using an ultrapure water system.

### Fabrication of F−Cu catalyst

In a typical procedure, $Cu(NO_3)_2 \cdot 3H_2O$ (2.0 mmol) was added into DMF (50 mL), and then $NH_4HF_2$ (2.0 mmol) was added. After vigorous stirring for 30 min, the mixture was transferred into a Teflon-lined autoclave (100 mL). The autoclave was then sealed and heated at 160 °C for 4 h. After cooling to room

temperature, the solid product was collected and washed with ethanol and water, and then dried in vacuum at 60 °C overnight to obtain Cu(OH)F. To prepare the electrode, 10 mg samples were dispersed in 1.0 mL of isopropanol-water solution with a volume ratio of 3:1 by sonicating for 2 h to form a homogeneous ink. Then, a proper amount of the ink was loaded onto a 0.5 cm × 2 cm GDL to create a GDE. Finally, the electrode was reduced in 1.0 M KOH solution at −0.6 V versus RHE for 5 min. The mass loading of catalyst was controlled at 0.25 ± 0.05 mg $cm^{-2}$ by adjusting the catalyst ink amount. For this purpose, the weight difference of GDL before loading the catalyst ink and after electroreduction was measured by a micro balance.

**Fabrication of Cl−Cu, Br−Cu and I−Cu catalysts**

In a typical procedure, 300 mg $NH_4Cl$, $NH_4Br$ or $NH_4I$ was added into 50 mL ethanol-water solution with a volume ratio of 49:1, and then 50 mg Cu(OH)F was added. After vigorous stirring for 24 h, the solid products were collected and washed with ethanol and water, and then dried in vacuum at 60 °C overnight. The subsequent procedures for the preparation of GDE were the same as those for the preparation of F−Cu catalyst.

**Fabrication of Cu catalyst**

In a typical procedure, $Cu(NO_3)_2 \cdot 3H_2O$ (2.0 mmol) was added into DMF (50 mL). After vigorous stirring for 30 min, the mixture was transferred into a Teflon-lined autoclave (100 mL). The autoclave was then sealed and heated at 220 °C for 36 h. After cooling to room temperature, the solid products were collected and washed with ethanol and water, and then dried in vacuum at 60 °C overnight. The subsequent procedures for the preparation of the Cu electrode were the same as those for the preparation of F−Cu catalyst.

**Fabrication of Ni foam@NiFeO$_x$ nanosheet catalyst**

Ni foam@NiFeO$_x$ nanosheet catalyst was synthesized by an electrodeposition method reported previously[53]. Typically, the electrodeposition was carried out in a three-electrode configuration containing Ni foam as the working electrode, platinum plate as the counter electrode and Ag/AgCl as the reference electrode. The electrolyte was 3 mM $Ni(NO_3)_2$ and 3 mM $Fe(NO_3)_3$ aqueous solution. The electrodeposition was conducted at −1.0 V versus Ag/AgCl at 10 ºC for 5 min.

**Characterisation**

Powder X-ray diffraction (XRD) patterns were recorded on a Rigaku Ultima IV diffractometer using Cu $K_\alpha$ radiation (40 kV, 30 mA). Scanning electron microscopy (SEM) measurements were performed on a Hitachi S-4800 operated at 15 kV. High-resolution transmission electron microscopy (HRTEM) and energy-dispersive X-ray spectroscopy (EDX) measurements were carried out on a Phillips Analytical FEI Tecnai 20 electron microscope operated at an acceleration voltage of 200 kV. The X-ray photoelectron spectroscopy (XPS) and Auger spectroscopy measurements were performed in an ultrahigh vacuum system chamber equipped with an Omicron XPS. A Sphera II hemispherical electron energy analyser and a monochromatic Al $K_\alpha$ radiation (1486.6 eV) X-ray source were used. The gas adsorption isotherms were measured at 25 ºC with Magnetic Suspension Balance.

**Electrochemical measurements**

All electrochemical measurements were performed in a flow cell composed of a GDE, anion exchange membrane and Ni foam anode as shown in Supplementary Fig. 1. The electrolysis was controlled by a CHI 660e electrochemical workstation equipped with a high current amplifier CHI 680c. Saturated Ag/AgCl was

used as the reference, and it was calibrated with respect to RHE: $E$ (RHE) = $E$ (Ag/AgCl) + 0.197 + pH × 0.0592. All the electrocatalytic reactions were conducted at ambient pressure and temperature, and 85% IR correction was applied in all the measurements. The cell resistances ($R$) with different electrolytes were measured by electrochemical impedance spectroscopy under open circuit potentials and were displayed in Supplementary Table 6.

KOH was typically used as the electrolyte and was circulated through the electrochemical cell using a peristaltic pump. High purity $CO_2$ was supplied to the cathode with a constant flow rate monitored by a mass flow controller. Unless otherwise stated, the reaction was conducted in 1 M KOH with a flow rate of 10 mL $min^{-1}$ for 30 min, and the gas flow rate was 50 mL $min^{-1}$. During electrolytic reaction, the effluent gas from the cathode compartment went through the sampling loop of gas chromatograph and was analysed on line. $H_2$ was analysed by thermal conductivity detector (TCD). CO, methane and ethylene were analysed by flame ionization detector (FID). Liquid products (formate, acetate, ethanol and n-propanol) were analysed by $^1$H NMR spectroscopy. The $^1$H NMR spectrum was recorded on an Advance III 500-MHz Unity plus spectrometer (Bruker), in which 0.5 mL of the electrolyte was mixed with 0.1 mL DMSO (internal standard, diluted to 100 ppm (v/v) by deuterated water). The gaseous products were sampled and analysed online every 15 min during the reaction, and the averaged result was used for discussion. The liquid products were collected and analysed after the operation for 30 min. Electrocatalytic $CO_2$RR in $D_2O$ solution was performed with similar procedures except for replacing $H_2O$ with $D_2O$. The onset potential for CO (or ethylene) is the lowest potential required for its formation, at which the Faradaic efficiency for CO (or ethylene) is ~1%. The evaluation of $CO_2$RR performance is displayed in Supplementary Methods.

***In situ* XAS measurements**

The measurements were carried out at the BL14W1 beamline of the Shanghai Synchrotron Radiation Facility (SSRF) operated at 3.5 GeV with a constant current of 260 mA. The measurements at the Cu K-edge were performed in fluorescence mode using a Lytle detector. The electrolysis was performed in 1.0 M KOH with a reactant gas flow rate of 10 mL $min^{-1}$ in a two-compartment H-type cell. *In situ* XAS measurements were recorded at an applied potential of −0.6 V versus RHE for maintaining 1 h. The XAS data were analysed using the software package Athena.

***In situ* ATR-FTIRS measurements**

The catalyst ink was dropped via pipette onto a hemicylindrical silicon prism covered with two layers of graphene. A Pt foil and a SCE electrode were used as counter and reference electrodes, respectively. The electrolyte was 0.1 M $KHCO_3$, which was constantly purged with $CO_2$ during the experiment. Before the experiments, the working electrode was reduced to stable state by continuously scanning the electrode potential in the region from 0.6 to −0.9 V versus RHE at a scan rate of 50 mV $s^{-1}$ for 20 cycles. The electrode potential was held at 0.4 V versus RHE and a background spectrum (reflectance $R_0$) was recorded. The electrode potential was altered from −0.1 to −1.0 V versus RHE stepwise, and in the meantime IR spectra were recorded with a time resolution of 42 s per spectrum at a spectral resolution of 8 $cm^{-1}$. All spectra were reported as the relative change in reflectivity, $\Delta R/R_0 = (R-R_0)/R_0$, where $R$ and $R_0$ are single-beam spectra collected at the sample potential and the reference potential, respectively. A Nicolet 8700 infrared spectrometer with an HgCdTe detector cooled by liquid nitrogen was used.

**DFT calculations**

All calculations were performed on the Vienna ab initio simulation package (VASP 5.4.1), a plane-wave

DFT software package[54,55]. The 2003 version of projector-augmented wave (PAW) potentials[56] was used, and the detailed descriptions of the PAW potentials of different elements are displayed in Supplementary Table 7. The Perdew-Burke-Ernzerhof (PBE) functional within the generalized gradient approximation (GGA) was used to calculate the electron exchange and correlation energies[57,58]. The Cu(111) with 4 × 4 four-layer slab was used as the model surface, a main exposed facet in our experimental result. The bottom two layers were fixed and the vacuum space was 20 Å to avoid interactions with their periodic images. The 3 × 3 × 1 Monkhorst-Pack k-point meshes and a plane-wave cutoff energy of 450 eV were used in all calculations[59]. The structure converges until all the forces on the free atoms were less than 0.05 eV/Å. Considering that entropic effect is rather small for surface reactions (Supplementary Note 3 and Supplementary Table 8), we used reaction total energies for discussion. The constrained optimization method[60] was used to search for the structures of transition states, which were confirmed to have only one imaginary frequency based on the finite displacement method. The Cu 2p core-level binding energy shift was calculated using the VASP code with the final state approximation[61]. The calculated Cu 2p core-level binding energy shift in the presence of F on Cu was +0.1 eV compared to pure Cu, in agreement with the XPS result (Supplementary Fig. 18a). The calculations of phase diagram and core-level binding energy shift are displayed in Supplementary Methods. The atomic coordinates of the optimized computational models are provided in Supplementary Data 1.

**Data availability.** The data supporting the findings of this study are available within the article and its supplementary information files. Additional data are available from the corresponding authors on reasonable request.

**References**


1. Olah, G. A., Prakash, G. K. S. & Goeppert, A. Anthropogenic chemical carbon cycle for a sustainable future. *J. Am. Chem. Soc.* **133**, 12881-12898 (2011).
2. Centi, G., Quadrelli, E. A. & Perathoner, S. Catalysis for $CO_2$ conversion: a key technology for rapid introduction of renewable energy in the value chain of chemical industries. *Energy Environ. Sci.* **6**, 1711-1731 (2013).
3. Aresta, M., Dibenedetto, A. & Angelini, A. Catalysis for the valorization of exhaust carbon: from $CO_2$ to chemicals, materials, and fuels. Technological use of $CO_2$. *Chem. Rev*. **114**, 1709-1742 (2014).
4. Bushuyev, O. S. et al. What should we make with $CO_2$ and how can we make it? *Joule* **2**, 825-832 (2018).
5. Yang, H. et al. A review of the catalytic hydrogenation of carbon dioxide into value-added hydrocarbons. *Catal. Sci. Technol.* **7**, 4580-4598 (2017).
6. Guo, L., Sun, J., Ge, Q. & Tsubaki, N. Recent advances in direct catalytic hydrogenation of carbon dioxide to valuable $C_{2+}$ hydrocarbons. *J. Mater. Chem. A* **6**, 23244-23262 (2018).
7. Dokania, A., Ramirez, A., Bavykina, A. & Gascon, J. Heterogeneous catalysis for the valorization of $CO_2$: role of bifunctional processes in the production of chemicals. *ACS Energy Lett.* **4**, 167-176 (2019).
8. Zhou, W. et al. New horizon in C1 chemistry: breaking the selectivity limitation in transformation of syngas and hydrogenation of $CO_2$ into hydrocarbon chemicals and fuels. *Chem. Soc. Rev.* **48**, 3193-3228 (2019).
9. Porosoff, M. D., Yan, B. & Chen, J. G. Catalytic reduction of $CO_2$ by $H_2$ for synthesis of

CO, methanol and hydrocarbons: challenges and opportunities. *Energy Environ. Sci.* **9**, 62-73 (2016).

10. De Luna, P. et al. What would it take for renewably powered electrosynthesis to displace petrochemical processes? *Science* **364**, 350-358 (2019).
11. Tackett, B. M., Gomez, E. & Chen, J. G. Net reduction of $CO_2$ via its thermocatalytic and electrocatalytic transformation reactions in standard and hybrid processes. *Nat. Catal.* **2**, 381-386 (2019).
12. Nielsen, D. U., Hu, X. M., Daasbjerg, K. & Skrydstrup, T. Chemically and electrochemically catalysed conversion of $CO_2$ to CO with follow-up utilization to value-added chemicals. *Nat. Catal.* **1**, 244-254 (2018).
13. Schouten, K. J. P. et al. A new mechanism for the selectivity to $C_1$ and $C_2$ species in the electrochemical reduction of carbon dioxide on copper electrodes. *Chem. Sci.* **2**, 1902-1909 (2011).
14. Kuhl, K. P., Cave, E. R., Abram, D. N. & Jaramillo, T. F. New insights into the electrochemical reduction of carbon dioxide on metallic copper surfaces. *Energy Environ. Sci.* **5**, 7050-7059 (2012).
15. Gao, D., Arán-Ais, R. M., Jeon, H. S. & Roldan Cuenya, B. Rational catalyst and electrolyte design for $CO_2$ electroreduction towards multicarbon products. *Nat. Catal.* **2**, 198-210 (2019).
16. Qiao, J., Liu, Y., Hong, F. & Zhang, J. A review of catalysts for the electroreduction of carbon dioxide to produce low-carbon fuels. *Chem. Soc. Rev.* **43**, 631-675 (2014).
17. Nitopi, S. et al. Progress and perspectives of electrochemical $CO_2$ reduction on copper in

aqueous electrolyte. *Chem. Rev.* **119**, 7610-7672 (2019).

18. Loiudice, A. et al. Tailoring copper nanocrystals towards $C_2$ products in electrochemical $CO_2$ reduction. *Angew. Chem. Int. Ed.* **55**, 5789-5792 (2016).
19. De Luna, P. et al. Catalyst electro-redeposition controls morphology and oxidation state for selective carbon dioxide reduction. *Nat. Catal.* **1**, 103-110 (2018).
20. Jiang, K. et al. Metal ion cycling of Cu foil for selective C–C coupling in electrochemical $CO_2$ reduction. *Nat. Catal.* **1**, 111-119 (2018).
21. Zhuang, T. T. et al. Steering post-C–C coupling selectivity enables high efficiency electroreduction of carbon dioxide to multi-carbon alcohols. *Nat. Catal.* **1**, 421-428 (2018).
22. Zhou, Y. et al. Dopant-induced electron localization drives $CO_2$ reduction to $C_{2+}$ hydrocarbons. *Nat. Chem.* **10**, 974-980 (2018).
23. Ren, D., Ang, B. S. H. & Yeo, B. S. Tuning the selectivity of carbon dioxide electroreduction toward ethanol on oxide-derived $Cu_xZn$ Catalysts. *ACS Catal.* **6**, 8239-8247 (2016).
24. He, J. et al. High-throughput synthesis of mixed-metal electrocatalysts for $CO_2$ reduction. *Angew. Chem. Int. Ed.* **56**, 6068-6072 (2017).
25. Hoang, T. T. H. et al. Nanoporous copper-silver alloys by additive-controlled electrodeposition for the selective electroreduction of $CO_2$ to ethylene and ethanol. *J. Am. Chem. Soc.* **140**, 5791-5797 (2018).
26. Morales-Guio, C. G. et al. Improved $CO_2$ reduction activity towards $C_{2+}$ alcohols on a tandem gold on copper electrocatalyst. *Nat. Catal.* **1**, 764-771 (2018).
27. Varela, A. S., Ju, W., Reier, T. & Strasser, P. Tuning the catalytic activity and selectivity of

Cu for $CO_2$ electroreduction in the presence of halides. *ACS Catal.* **6**, 2136-2144 (2016).

28. Dinh, C. T. et al. $CO_2$ electroreduction to ethylene via hydroxide-mediated copper catalysis at an abrupt interface. *Science* **360**, 783-787 (2018).
29. Gao, D., Scholten, F. & Roldan Cuenya, B. Improved $CO_2$ electroreduction performance on plasma-activated Cu catalysts via electrolyte design: halide effect. *ACS Catal.* **7**, 5112-5120 (2017).
30. Lv, J. J. et al. A highly porous copper electrocatalyst for carbon dioxide reduction. *Adv. Mater.* **30**, 1803111 (2018).
31. Jouny, M., Luc, W. & Jiao, F. High-rate electroreduction of carbon monoxide to multi-carbon products. *Nat. Catal.* **1**, 748-755 (2018).
32. Allen, L. C. Electronegativity is the average one-electron energy of the valence-shell electrons in ground-state free atoms. *J. Am. Chem. Soc.* **111**, 9003-9014 (1989).
33. Gabardo, C. M. et al. Combined high alkalinity and pressurization enable efficient $CO_2$ electroreduction to CO. *Energy Environ. Sci.* **11**, 2531-2539 (2018).
34. Zhou, H. et al. Fluoroalkyl silane modified silicone rubber/nanoparticle composite: a super durable, robust superhydrophobic fabric coating. *Adv. Mater.* **24**, 2409-2412 (2012).
35. Chang, X. et al. Tuning $Cu/Cu_2O$ interfaces for reduction of carbon dioxide to methanol in aqueous solutions. *Angew. Chem. Int. Ed.* **57**, 15415-15419 (2018).
36. Totir, G. G., Chottiner, G. S., Gross, C. L. & Scherson, D. A. XPS studies of the chemical and electrochemical behavior of copper in anhydrous hydrogen fluoride. *J. Electroanal. Chem.* **532**, 151-156 (2002).
37. Lee, W.-H., Byun, J., Cho, S. K. & Kim, J. J. Effect of halides on Cu electrodeposit film:

potential-dependent impurity incorporation. *J. Electrochem. Soc.* **164**, 493-497 (2017).

38. Kau, L. S., Spira-Solomon, D. J., Penner-Hahn, J. E., Hodgson, K. O. & Solomon, E. I. X-ray absorption edge determination of the oxidation state and coordination number of copper. Application to the type 3 site in Rhus vernicifera laccase and its reaction with oxygen. *J. Am. Chem. Soc.* **109**, 6433-6442 (1987).
39. Huang, Y., Handoko, A. D., Hirunsit, P. & Yeo, B. S. Electrochemical reduction of $CO_2$ using copper single-crystal surfaces: effects of ∗CO coverage on the selective formation of ethylene. *ACS Catal.* **7**, 1749-1756 (2017).
40. Sandberg, R. B., Montoya, J. H., Chan, K. & Nørskov, J. K. CO–CO coupling on Cu facets: Coverage, strain and field effects. *Surf. Sci.* **654**, 56-62 (2016).
41. Reuter, K. & Scheffler, M. Composition, structure, and stability of $RuO_2$(110) as a function of oxygen pressure. *Phys. Rev. B* **65**, 035406 (2001).
42. Montoya, J. H., Peterson, A. A. & Nørskov, J. K. Insights into C–C coupling in $CO_2$ electroreduction on copper electrodes. *ChemCatChem* **5**, 737-742 (2013).
43. Gao, D. et al. Selective $CO_2$ electroreduction to ethylene and multicarbon alcohols via electrolyte-driven nanostructuring. *Angew. Chem. Int. Ed.* **58**, 17047-17053 (2019).
44. Gao, S. et al. Partially oxidized atomic cobalt layers for carbon dioxide electroreduction to liquid fuel. *Nature* **529**, 68-71 (2016).
45. Li, C. W., Ciston, J. & Kanan, M. W. Electroreduction of carbon monoxide to liquid fuel on oxide-derived nanocrystalline copper. *Nature* **508**, 504-507 (2014).
46. Subbaraman, R. et al. Enhancing hydrogen evolution activity in water splitting by tailoring $Li^+$-$Ni(OH)_2$-Pt interfaces. *Science* **334**, 1256-1260 (2011).

47. Ma, W. et al. Promoting electrocatalytic $CO_2$ reduction to formate via sulfur-boosting water activation on indium surfaces. *Nat. Commun.* **10**, 892 (2019).

48. Staszak-Jirkovský, J. et al. Design of active and stable Co-Mo-$S_x$ chalcogels as pH-universal catalysts for the hydrogen evolution reaction. *Nat. Mater.* **15**, 197-203 (2015).

49. Cheng, T., Xiao, H. & Goddard III, W. A. Reaction mechanisms for the electrochemical reduction of $CO_2$ to CO and formate on the Cu (100) surface at 298 K from quantum mechanics free energy calculations with explicit water. *J. Am. Chem. Soc.* **138**, 13802-13805 (2016).

50. Wuttig, A. et al. Tracking a common surface-bound intermediate during $CO_2$-to-fuels catalysis. *ACS Cent. Sci.* **2**, 522-528 (2016).

51. Krauth, O., Fahsold, G., Magg, N. & Pucci, A. Anomalous infrared transmission of adsorbates on ultrathin metal films: Fano effect near the percolation threshold. *J. Chem. Phys.* **113**, 6330-6333 (2000).

52. Lu, G. Q. et al. In situ FTIR spectroscopic studies of adsorption of CO, $SCN^-$, and poly (o-phenylenediamine) on electrodes of nanometer thin films of Pt, Pd, and Rh: Abnormal infrared effects (AIREs). *Langmuir* **16**, 778-786 (2000).

53. Lu, X. & Zhao, C. Electrodeposition of hierarchically structured three-dimensional nickel-iron electrodes for efficient oxygen evolution at high current densities. *Nat. Commun.* **6**, 6616 (2015).

54. Kresse, G. & Joubert, D. From ultrasoft pseudopotentials to the projector augmented-wave method. *Phys. Rev. B* **59**, 1758-1775 (1999).

55. Kresse, G. & Furthmüller, J. Efficiency of ab-initio total energy calculations for metals and

semiconductors using a plane-wave basis set. *Comput. Mater. Sci.* **6**, 15-50 (1996).

56. Lejaeghere, K. et al. Reproducibility in density functional theory calculations of solids. *Science* **351**, aad3000 (2016).
57. Perdew, J. P. et al. Atoms, molecules, solids, and surfaces: Applications of the generalized gradient approximation for exchange and correlation. *Phys. Rev. B* **46**, 6671-6687 (1992).
58. Perdew, J. P., Burke, K. & Ernzerhof, M. Generalized gradient approximation made simple. *Phys. Rev. Lett.* **77**, 3865-3868 (1996).
59. Pack, J. D. & Monkhorst, H. J. Special points for Brillonln-zone integrations-a reply. *Phys. Rev. B* **16**, 1748-1749 (1977).
60. Wang, H. & Liu, Z. Comprehensive mechanism and structure-sensitivity of ethanol oxidation on platinum: New transition-state searching method for resolving the complex reaction network. *J. Am. Chem. Soc.* **130**, 10996-11004 (2008).
61. Köhler, L. & Kresse, G. Density functional study of CO on Rh (111). *Phys. Rev. B* **70**, 165405 (2004).

**Acknowledgements**

This work was supported by the National Key Research and Development Program of the Ministry of Science and Technology of China (No. 2017YFB0602201), the National Natural Science Foundation of China (Nos. 21690082, 91545203, 21503176 and 21802110), We thank staffs at the BL14W1 beamline of the Shanghai Synchrotron Radiation Facilities (SSRF) for assistance with the EXAFS measurements.

**Author contributions**

W.M. and S.X. performed most of the experiments and analysed the experimental data. T.L. and Q. F. performed computational studies and analysed the computational data. J.Y conducted ATR-FTIRS measurements and analysed the results. F.S. and Z.J. conducted XAS measurements and analysed the results. Q.Z. analysed all the data and co-wrote the paper. J.C. guided the computational work, analysed all the data and co-wrote the paper. Y.W. designed and guided the study, and co-wrote the paper. All of the authors discussed the results and reviewed the manuscript.

**Competing interests:** The authors declare no competing interests.

**Additional information**

**Supplementary Information** accompanies this paper at https://doi.org/

**Reprints and permissions** information is available at www.nature.com/reprints.

**Publisher's note:** Springer Nature remains neutral with regard to jurisdictional claims in published maps and institutional affiliations.

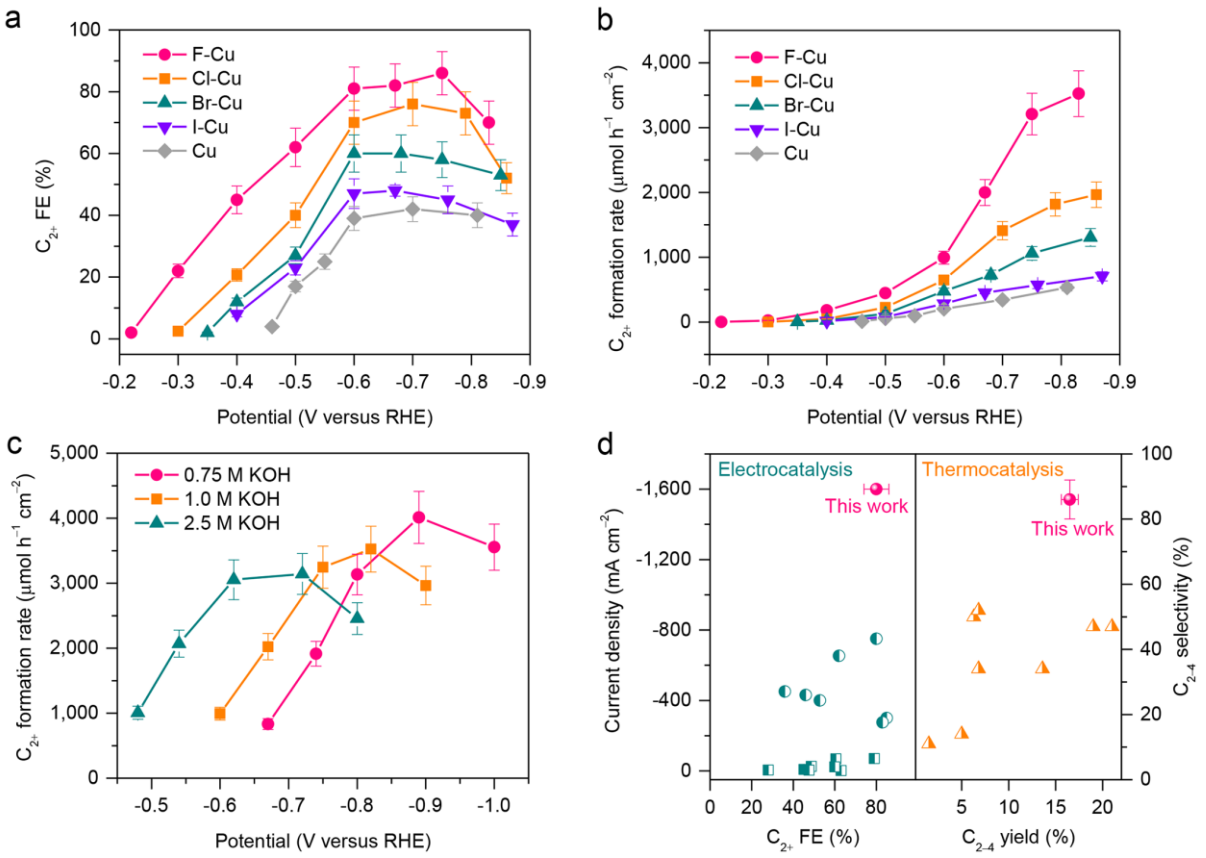


**Fig. 1 | Electrocatalytic $CO_2$RR performances. a,** FEs of $C_{2+}$ products under different applied potentials over X–Cu catalysts in 1.0 M KOH. **b,** Formation rates of $C_{2+}$ products under different applied potentials over X–Cu catalysts in 1.0 M KOH. **c,** Formation rates of $C_{2+}$ products over F–Cu catalyst in KOH with different concentrations. **d,** Comparison of some typical electrocatalytic and thermocatalytic systems reported to date (see Supplementary Tables 2-3 for details). The square and circle in Fig. 1d represent the reactions conducted in H-cell and in flow cell, respectively. The experiments in each case were performed in triplicates and the results are shown as mean ± standard deviation.

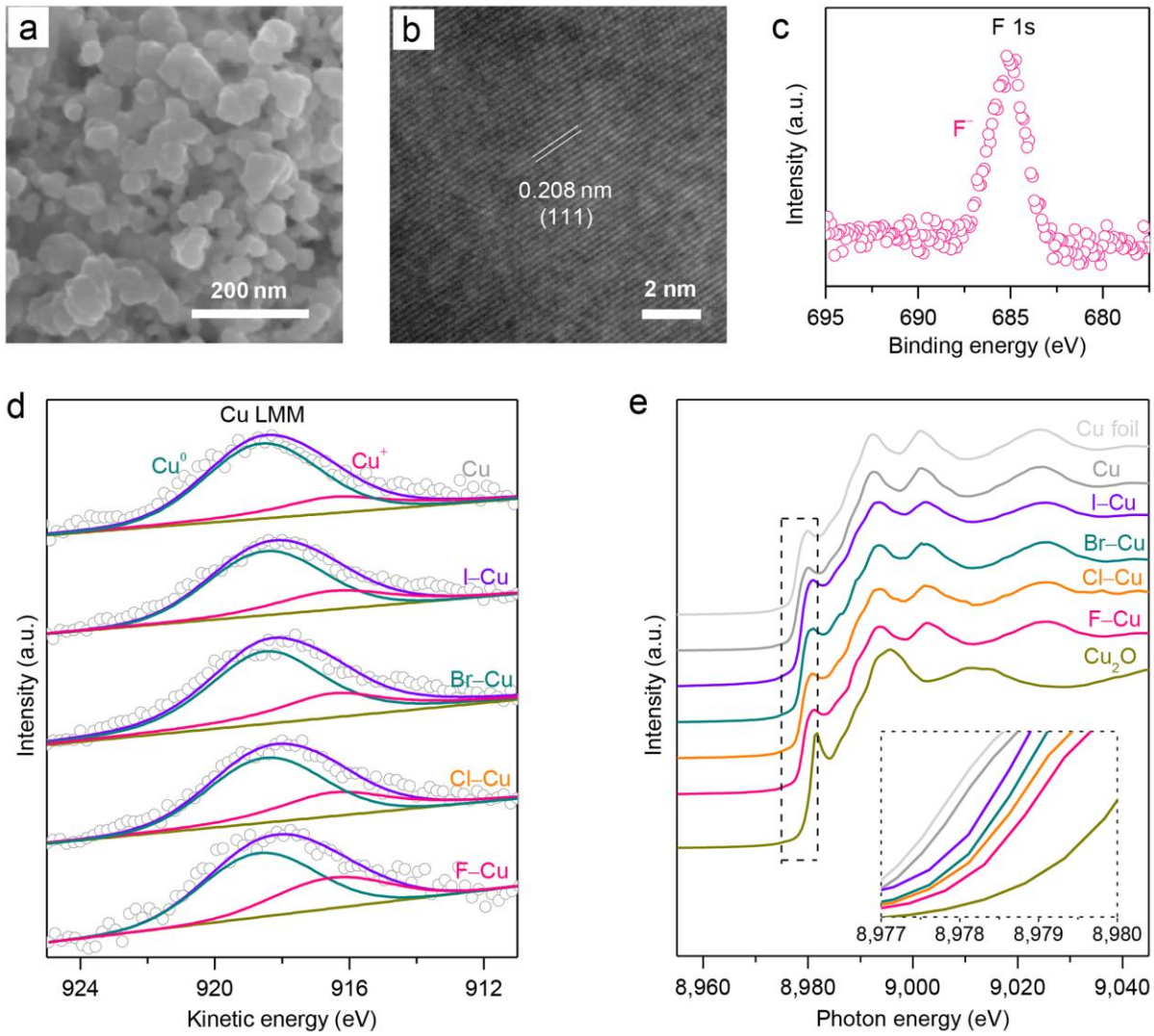


**Fig. 2 | Morphologies and chemical states of X−Cu catalysts. a,** SEM image of F−Cu catalyst. **b,** HRTEM image of F−Cu catalyst. **c,** F 1s XPS spectrum of F−Cu catalyst. **d,** Cu LMM Auger spectra of X−Cu catalysts. **e,** *In situ* Cu K-edge XANES spectra of X−Cu catalysts at −0.6 V versus RHE in 1.0 M KOH.

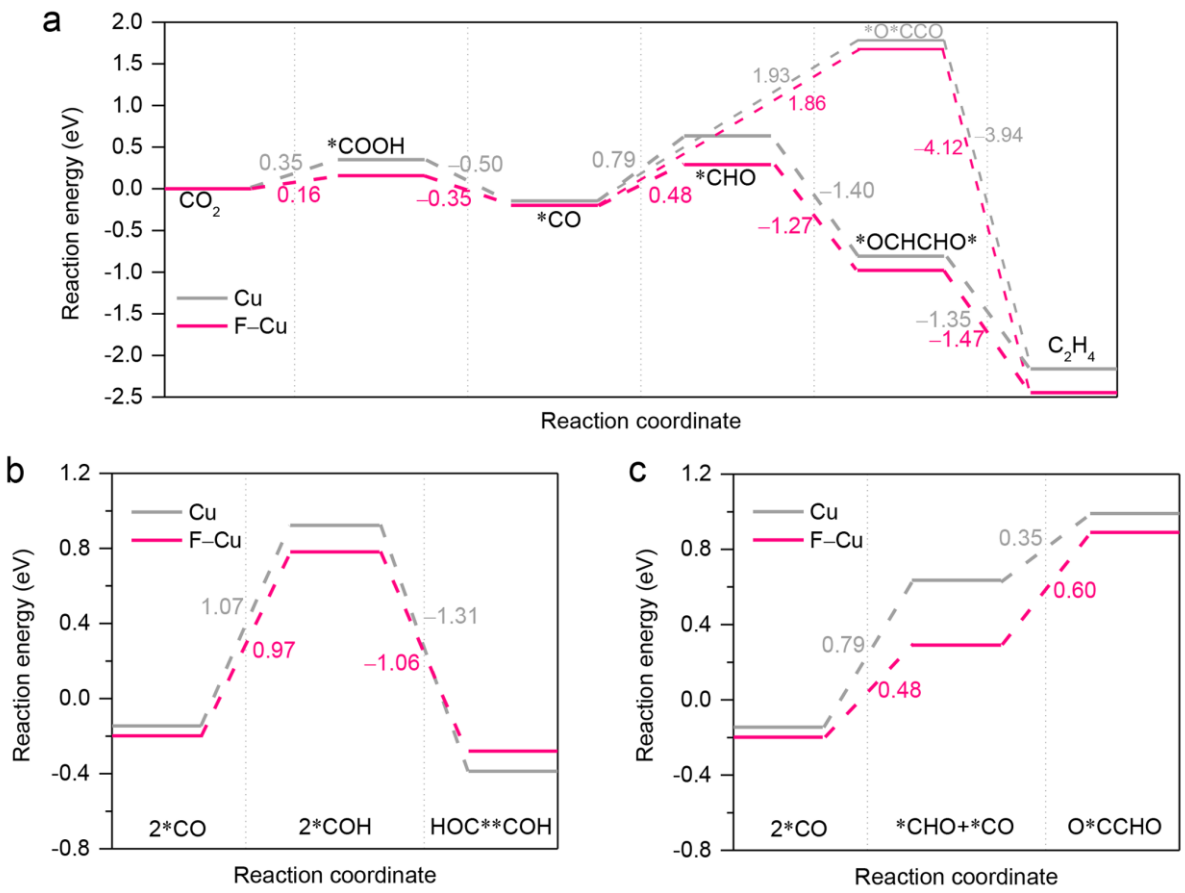


**Fig. 3 | DFT calculation results. a,** Reaction energy diagram for $CO_2RR$ to $C_2H_4$ via direct ∗CO dimerization pathway or ∗CO hydrogenation to ∗CHO followed by dimerization pathway on Cu(111) and F−Cu(111) facets. **b**, Reaction energy diagram for ∗CO hydrogenation to ∗COH, and subsequent dimerization to HOC∗∗COH on Cu(111) and F−Cu(111) facets. **c**, Reaction energy diagram for ∗CO hydrogenation to ∗CHO, and subsequent coupling with another ∗CO to O∗CCHO on Cu(111) and F−Cu(111) facets.

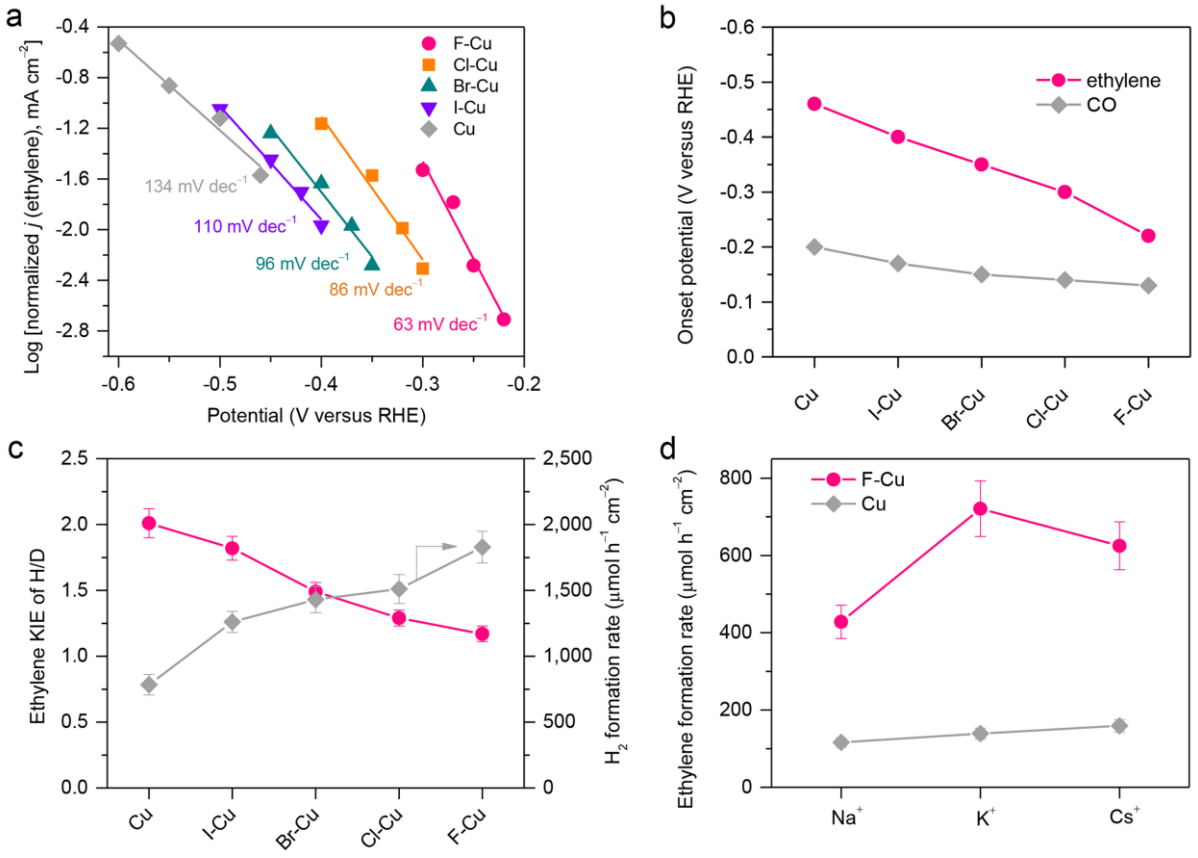


**Fig. 4 | Functioning mechanism of halogen on X−Cu catalysts. a,** Tafel plots. **b,** Onset potentials for CO and $C_2H_4$. **c,** KIE of H/D in $CO_2RR$ to ethylene and hydrogen evolution performance under Ar atmosphere at −0.6 V versus RHE. **d,** Effect of alkali metal cations in MOH (M = $Na^+$, $K^+$ and $Cs^+$) electrolyte on $CO_2RR$ to $C_2H_4$ at −0.6 V versus RHE over Cu and F−Cu catalysts. The experiments in each case were performed in triplicates and the results are shown as mean ± standard deviation.

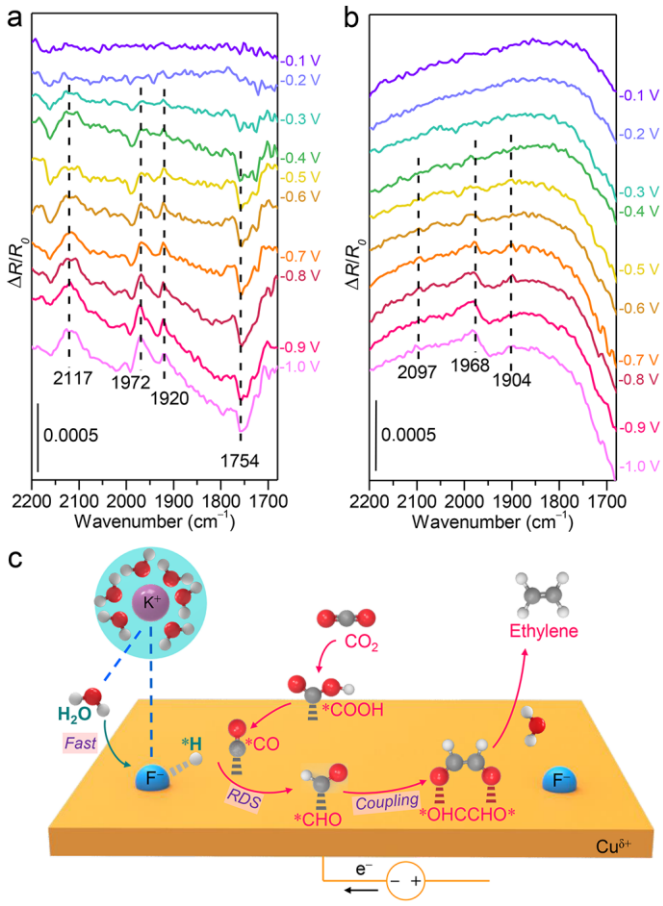


**Fig. 5 | *In situ* ATR-FTIRS and reaction scheme. a,** *In situ* ATR-FTIRS recorded at different applied potentials for F−Cu catalyst in 0.1 M $KHCO_3$ electrolyte. **b,** *In situ* ATR-FTIRS recorded at different applied potentials for Cu catalyst in 0.1 M $KHCO_3$ electrolyte. $\Delta R/R_0 = (R-R_0)/R_0$, where $R$ and $R_0$ are single-beam spectra collected at the sample potential and the reference potential, respectively. Normally, IR absorption of surface species decreases the reflection intensity, thus the generation of species yields downward peak, such as ∗CHO at 1754 $cm^{-1}$. For ∗CO species, the inversion of peak was observed, named abnormal infrared effects, probably due to the adsorbate vibrational excitation interacting with electronic excitation[51,52]. **c,** Proposed reaction mechanism for $CO_2$RR to $C_2H_4$. The purple, blue, red, grey and white balls represent K, F, O, C and H, respectively.